Effect of hafnium and molybdenum addition on inclusion characteristics in Co-based dual-phase high-entropy alloys

Yong Wang[1,2], *Wei Wang*[3],✉, *Joo Hyun Park*[4], *and Wangzhong Mu*[2,5],✉

1) Key Laboratory for Ferrous Metallurgy and Resources Utilization of Ministry of Education & Hubei Provincial Key Laboratory for New Processes of Ironmaking and Steelmaking, Wuhan University of Science and Technology, Wuhan 430081, China

2) Department of Materials Science and Engineering, KTH Royal Institute of Technology, SE-100 44, Stockholm, Sweden

3) Department of Chemical Engineering, Northeast Electric Power University, Jilin 132012, China

4) Department of Materials Science and Chemical Engineering, Hanyang University, Ansan 15588, Korea

5) Engineering Materials, Division of Materials Science, Department of Engineering Science and Mathematics, Luleå University of Technology, 97187 Luleå, Sweden

Abstract: Specific grades of high-entropy alloys (HEAs) can provide opportunities for optimizing properties toward high-temperature applications. In this work, the Co-based HEA with a chemical composition of $Co_{47.5}Cr_{30}Fe_{7.5}Mn_{7.5}Ni_{7.5}$ (at%) was chosen. The refractory metallic elements hafnium (Hf) and molybdenum (Mo) were added in small amounts (1.5at%) because of their well-known positive effects on high-temperature properties. Inclusion characteristics were comprehensively explored by using a two-dimensional cross-sectional method and extracted by using a three-dimensional electrolytic extraction method. The results revealed that the addition of Hf can reduce Al_2O_3 inclusions and lead to the formation of more stable Hf-rich inclusions as the main phase. Mo addition cannot influence the inclusion type but could influence the inclusion characteristics by affecting the physical parameters of the HEA melt. The calculated coagulation coefficient and collision rate of Al_2O_3 inclusions were higher than those of HfO_2 inclusions, but the inclusion amount played a larger role in the agglomeration behavior of HfO_2 and Al_2O_3 inclusions. The impurity level and active elements in HEAs were the crucial factors affecting inclusion formation.

Keywords: high-entropy alloy; non-metallic inclusion; agglomeration; thermodynamics; alloying

1. Introduction

High-entropy alloys (HEAs) have a wide composition range, which is attractive for designing new alloys [1–3]. Occasionally, single-phase entropic alloys show remarkable damage tolerance, i.e., high tensile strength and impact toughness at cryogenic temperatures [4]; however, they can exhibit a large loss of ductility with a decrease in temperature in tensile tests. In recent years, the alloy design strategy has been to make the dual-phase HEA overcome the strength–ductility trade-off [5–7]. This change allows the development of a dual-phase microstructure where both phases have the maximum benefit of the solid-solution strengthening effect, and one phase experiences deformation-induced martensitic transformation. In light of this, a specific grade Co-based dual-phase $Co_{47.5}Cr_{30}Fe_{7.5}Mn_{7.5}Ni_{7.5}$ alloy was developed. Details of the alloy design can be found elsewhere [8].

It has been shown that the outstanding mechanical and chemical properties of HEAs are due to the intermetallic compounds of alloying elements [9–10], where Hf and Mo are two typical intermetallic structure forming elements. Ren *et al.* [11] observed that the compressive yield strength increased from 1273 to 2023 MPa when increasing the Hf content from 0at% to 6at% in $(AlCoCrFeNi)_{100-x}Hf_x$ HEAs due to the formation of the Laves phase. Shun *et al.* [12] reported that with an increase in the Mo content in $CoCrFeNiMo_x$, the alloy hardness, yield stress, and compressive strength increased because of the solid-solution strengthening of the face-centred cubic structure (fcc) matrix and the formation of the σ or (σ + μ) phases. Haas *et al.* [13] reported the influence of Hf (0.5at%) and Mo (1.0at%) additions on the microstructural and mechanical properties of $Al_{10}Co_{25}Cr_8Fe_{15}Ni_{36}Ti_6$. They found that Mo addition decreased the ultimate tensile strength of the base alloy because of the more spherical morphology of γ′-particles, while Hf addition increased the ultimate tensile strength. Thus, a small amount of Hf and Mo (1.5at%) was added to the aforementioned Co-based HEA, which can promote the formation of the second phase and further modify the mechanical proper-

---

✉ Corresponding authors: Wangzhong Mu   E-mail: wmu@kth.se, wangzhongmu6699@gmail.com;
              Wei Wang   E-mail: wei6@kth.se

1640

Int. J. Miner. Metall. Mater., Vol. 31 , No. 7, Jul. 2024

ties of the alloy.

However, except for the effects of Hf and Mo on the microstructure and mechanical properties of HEAs, the utilization of these elements is also challenging because it may introduce complex non-metallic inclusions. $MnCr_2O_4$ oxide inclusions are commonly found in CrMnFeCoNi alloys [14–17], and their influence on mechanical properties has been ignored because of their small volume fraction. Yu *et al.* [18] reported that stable $MnO–SiO_2$ was formed in Si-added CoCrFeMnNi instead of the harmful $MnCr_2O_4$, which greatly enhanced the corrosion resistance of the alloy. Similarly, the stable inclusions can transform from $MnCr_2O_4$ inclusions to $Mn(Cr,Al)_2O_4$ inclusions and then to pure Al_2O_3 inclusions with increasing Al content in HEA [19]. Moreover, $MnCr_2O_4$ was also formed in $(CoCrFeMnNi)_{88}Mo_{12}$ and $CoCrFeNiMo_x$ alloys [12,20], which demonstrates that Mo addition has little effect on the inclusion type in HEAs. In terms of the effect of Hf, one of the most reactive elements, HfO_2 oxide, can be easily formed in different alloys [21–23], and the impurities and inclusions were determined as a function of the melting method [24]. (Ti,Hf)S hafnium and titanium sulfides and $(Ti,Hf)_2SC$ titanium and hafnium carbosulfides were found in Fe–Co–Ni–Cu–Al–Ti–Hf alloys with high sulfur contents (0.12wt%–0.32wt%) [24]. Moreover, it was revealed that the impurity element levels, as well as the active element, are the key challenges in controlling the inclusion phase in HEAs [25]. However, no systematic research on inclusions has been reported for Mo- and Hf-alloyed HEAs.

In this work, Hf- and Mo-alloyed HEAs were prepared by a combined vacuum arc melting–induction melting method. The systematic study of the alloying effects of Mo and Hf on the microstructure evolution and mechanical properties of HEAs will be reported in the future. This study focuses on the influence of alloy conditions on inclusion characteristics in Co-based HEAs. Moreover, the physical properties of the alloys associated with inclusion agglomeration behavior are discussed. This work offers a fundamental basis for future preparation of different alloyed HEAs.

2. Experimental

The reference HEA sample (hereafter Ref.-HEA) was prepared by a published method [19]. The HEA samples with Mo and Hf addition (denoted as Mo-HEA and Hf-HEA) were first synthesized by the vacuum arc melting method to melt all raw materials and subsequently remelted in an induction melting furnace. Raw metallic materials with a purity of over 99.95% were used, and the furnace chamber was flushed with high-purity Ar three times. The alloys were sub-

sequently remelted by induction heating to a temperature of 1550°C and held for 5 min. Finally, the samples were held and solidified in an Al_2O_3 crucible, which resulted in some trace amounts of Al in the alloys. The basic composition is $Co_{47.5}Cr_{30}Fe_{7.5}Ni_{7.5}Mn_{7.5}$, which was designed to include both fcc and hexagonal close packed (hcp) phases [6,25]. The chemical compositions of metallic elements in HEAs were examined by inductively coupled plasma optical emission spectrometry (ICP-OES), the contents of sulfur, oxygen, and nitrogen were determined using the LECO combustion analyzer. Detailed chemical compositions and impurity elements of each sample are summarized in Table 1.

Inclusions were first examined by using the two-dimensional (2D) method on the polished surface of HEA samples. To gather more precise information on inclusion morphologies and size distributions, three-dimensional (3D) observation by electrolytic extraction was performed. For the electrolytic extraction experiment, an electrolyte of 10vol% AA solution (10vol% acetylacetone, 1vol% tetramethylammonium chloride, and methanol), an average current of 50 mA, and an average voltage of 4 V were employed. The extracted inclusions in the solutions were filtered through a polycarbonate (PC) membrane film filter with a pore size of 0.4 μm. The inclusions on the filter were subsequently evaluated by scanning electron microscopy (SEM, JEOL JSM-7800F & Hitachi S3700N) equipped with energy-dispersive X-ray spectroscopy (EDS). The numbers of different types of inclusions per unit volume (N_v) in the alloys were determined, and the details are described elsewhere [19].

3. Results and discussion

3.1. Characterizations of inclusions in the three HEAs

Representative 2D and 3D morphologies of inclusions observed in Ref.-HEA are displayed in Fig. 1. It is found that most Mn(S,Se) inclusions have an irregular shape on the polished cross-sectional surface and have a dendrite shape by using the 3D method. The maximum length of the primary dendrite was approximately 60 μm, which was quite large compared with the 2D observations because some parts of the dendrite were not visible by the cross-section polishing method. Moreover, some globular or angular Mn(S,Se) inclusions were also observed, as reported in our previous work [19]. Se was contaminated in electrolytic manganese since SeO_2 is commonly used as an additive in aqueous electrolysis, and parts of Se were not completely removed during the production process. Moreover, MnS and MnSe can easily form Mn(S,Se) solid solutions because they have the same NaCl-type cubic structure. Spherical and globular Al_2O_3 in-

Table 1. Chemical composition of the principal elements and impurity levels of the three alloys

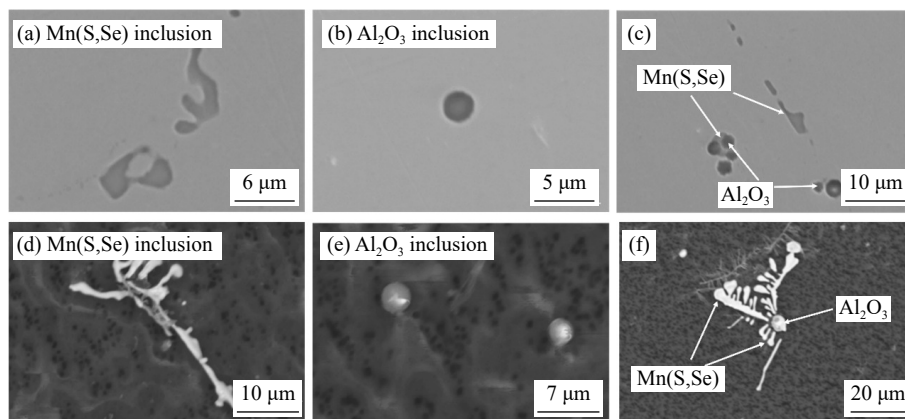| Sample	Alloying elements / at% (wt%)							Impurity / wt%			
	Co	Cr	Fe	Mn	Ni	Mo	Hf	Al	S	O	N
Ref.-HEA	Bal.	28.59 (26.34)	7.32 (7.24)	6.98 (6.79)	7.92 (8.24)			0.07	0.004	0.016	0.01
Mo-HEA	Bal.	31.95 (29.26)	7.85 (7.72)	4.67 (4.52)	8.02 (8.29)	1.38 (2.33)		0.08	0.005	0.012	0.01
Hf-HEA	Bal.	30.02 (26.86)	7.52 (7.53)	7.24 (6.84)	7.50 (7.57)		1.61 (4.63)	0.02	0.004	0.015	0.01

Fig. 1.   Typical inclusions observed by (a–c) 2D method and (d–f) 3D method in Ref.-HEA.

clusions were found by 2D and 3D methods, respectively. A small amount of polyhedral Al_2O_3 inclusions was also observed, and they easily formed aggregated clusters; the experimental evidence can be seen subsequently in this section. It should be mentioned that some irregular and dendritic $Mn(S,Se)$ inclusions precipitated on the surface of Al_2O_3 inclusions, as displayed in Fig. 1(c). Al_2O_3 inclusions usually serve as heterogeneous nucleation sites for the precipitation of $Mn(S,Se)$ inclusions during the solidification of the HEA melt. The experimental evidence can be seen thereafter in this section.

The SEM images of the typical inclusions in Mo-HEA are presented in Fig. 2. Two main types of inclusions, spherical $Mn(S,Se)$ and irregular Al_2O_3 inclusions, were observed. The 2D and 3D morphologies of the spherical $Mn(S,Se)$ inclusions with an average diameter of 2 μm are shown in Fig. 2(a) and (d), respectively. Irregular Al_2O_3 inclusions exhibited typical polygonal shapes in 3D observation (Fig. 2(e)). Moreover, many aggregated Al_2O_3 inclusions were observed (Fig. 2(b), (c), and (f)) and showed a much larger size than those in Ref.-HEA. In addition, polyhedral, plate, or irregular-shaped Al_2O_3 inclusions were found in the aggregate. The size difference can be attributed to the different physical properties of the HEA melt, which is discussed in detail in Section 3.3. It should be noted that complex inclusions with Al_2O_3 and $Mn(S,Se)$ were rarely observed in Mo-HEA, and the morphologies of $Mn(S,Se)$ inclusions were quite different from those in Ref.-HEA.

The representative morphologies of the inclusions in Hf-HEA are presented in Fig. 3. The overall distributions of Hf-containing particles are shown in Fig. 3(a), where they show a chain- or rodlike morphology with large size (Fig. 3(b)). The majority of particles are Hf-rich complex inclusions with some $Mn(S,Se)$. In addition, square-shaped Hf-oxide inclusions were also found (Fig. 3(c)), with a polygonal shape in the 3D method (Fig. 3(f)). Hereafter, this type of oxide inclusion is called HfO_2 since it is the only stable structure of hafnium oxide. It can be seen that most of the Hf-rich complex inclusions are in dendrite shape by the 3D method (Fig. 3(d)). In addition, the lengths of primary dendrites were occasionally larger than 30 μm, which are quite different from the 2D SEM morphologies. Aggregated Hf-rich complex inclusions and HfO_2 inclusions were commonly observed (Fig. 3(e)). The chemical elemental maps of inclusions in Ref.-HEA, Mo-HEA, and Hf-HEA are presented in Fig. 4(a) to (d). It is seen that the some sulfides comprising $Hf(S,Se)_2 + Mn(S,Se)$ were also found in Hf-HEA, as shown in the mapping results. It is interesting to note that these sulfide inclusions are at the tip of the dendritic Hf-rich complex inclusion. In addition, no single sulfides were found in the Hf-HEA, and the size and amount of these sulfides were much smaller than those of the Hf-rich inclusions. Therefore, only the characteristics of Hf-rich inclusions (Hf-rich complex inclusions + HfO_2 inclusions) were analyzed in this HEA.

Previous work has shown that the $MnCr_2O_4$ spinel is a stable inclusion in $Co_{85-x}Cr_xMn_{7.5}Ni_{7.5}$ and $Co_{77.5-x}Cr_xFe_{7.5}$
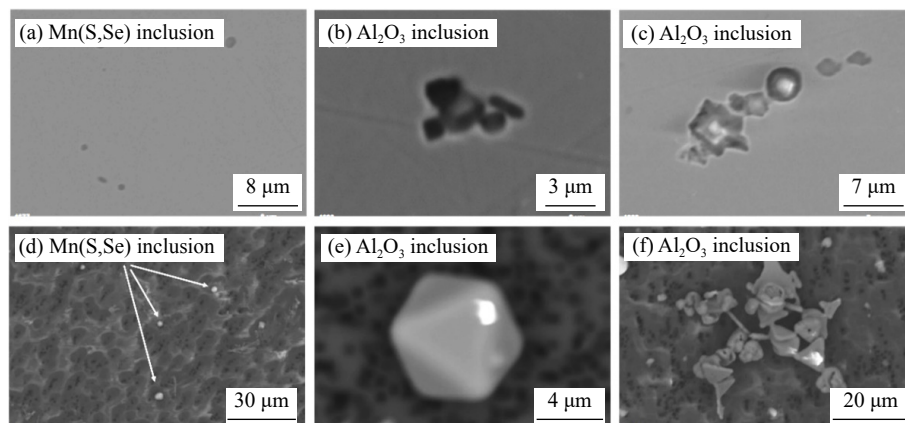

Fig. 2.   Typical inclusions observed by (a–c) 2D method and (d–f) 3D method in Mo-HEA.
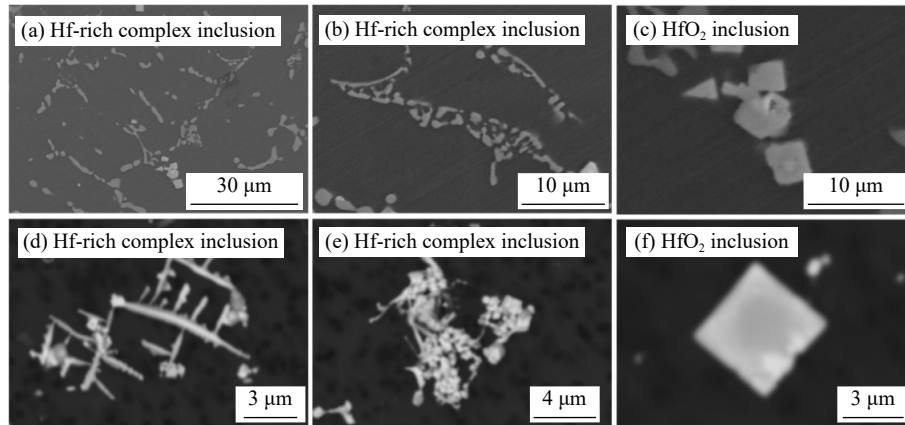
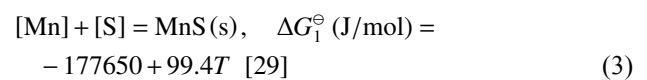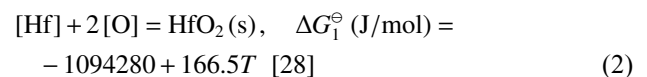**Fig. 3. Typical inclusions observed by (a–c) 2D method and (d–f) 3D method in Hf-HEA.**
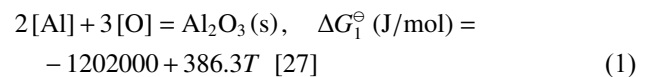
$Mn_{7.5}Ni_{7.5}$ (x = 15, 30) alloys without Al contamination [25]. The introduction of Al from the crucible materials led to the formation of Al_2O_3 inclusions in $Co_{47.5}Cr_{30}Fe_{7.5}Ni_{7.5}Mn_{7.5}$ alloy [19]. In this study, Al_2O_3 is a stable oxide inclusion in Ref.-HEA and Mo-HEA, whereas Hf-rich inclusions are more stable in Hf-HEA. In conclusion, Mo addition does not affect inclusion types, and Hf addition can cause the formation of stable Hf-rich inclusions. The formation of inclusions highly depends on the presence of active elements in the HEA melt, which is discussed in detail by thermodynamic calculations in Section 3.2. Furthermore, both Al_2O_3 and Hf-rich inclusions easily form clusters in HEA melt with quite different size ranges, which are associated with the properties of these inclusions and the difference in the physical properties of HEA melt.

The number density and size distributions of the inclusions in the three alloys are presented in Fig. 5. In terms of oxides, the number density of Al_2O_3 inclusions in Mo-HEA is larger than that in Ref.-HEA. Interestingly, most Al_2O_3 inclusions have a smaller size (less than 6 μm), with the maximum at about 12 μm in Ref.-HEA. The size range of Al_2O_3 inclusions is much wider in Mo-HEA, demonstrating that the size of Al_2O_3 inclusions is larger in Mo-HEA than in Ref.-HEA. The number density of Hf-rich inclusions in Hf-HEA is almost twice that of Al_2O_3 inclusions in Mo-HEA. The size range and maximum size of Hf-rich inclusions in Hf-HEA are also larger than those of Al_2O_3 inclusions in Ref.-HEA and Mo-HEA. It was revealed that fatigue crack initiation at the compact Al_2O_3 inclusion cluster resulted in a much higher fatigue life than initiation due to the large HfO_2 inclusion clusters under the same stress condition [26]. Based on this perspective, Hf-rich aggregates are more harmful than Al_2O_3 inclusions; therefore, inclusion characteristics should be carefully considered in Hf-containing HEAs. Regarding Mn(S,Se) inclusions, they show an opposite tendency to Al_2O_3 inclusions. Specifically, the number density of Mn(S,Se) inclusions in Ref.-HEA is slightly higher than that in Mo-HEA, which may be attributed to higher Mn and S contents in Ref.-HEA. Moreover, the size range of Mn(S,Se) inclusions in Ref.-HEA is about 1–32 μm, which is significantly larger than that in Mo-HEA (1–7 μm). Mo and Hf addition can cause a change in the physical parameters of the li-

quid alloys, which can lead to different characteristics in the number, density, and size range of inclusions. The details are discussed in Section 3.3.

3.2. Thermodynamic analysis of inclusion formation

As stated previously, different inclusion characteristics were obtained in the three entropic alloys depending on their compositions. Therefore, thermodynamic calculations were performed to theoretically understand the formation of inclusions in different HEA melts. It should be noted that HfS_2 inclusions were not considered due to the lack of thermodynamic data. Moreover, due to the complexity of Hf-rich inclusions, HfO_2 oxide was used to simplify the calculation process. The reactions in the HEA melt involving the impurity elements are shown below:

$$2\,[Al] + 3\,[O] = Al_2O_3\,(s), \quad \Delta G_1^{\ominus}\,(J/mol) =$$
$$-1202000 + 386.3T \quad [27] \tag{1}$$

$$[Hf] + 2\,[O] = HfO_2\,(s), \quad \Delta G_1^{\ominus}\,(J/mol) =$$
$$-1094280 + 166.5T \quad [28] \tag{2}$$

$$[Mn] + [S] = MnS\,(s), \quad \Delta G_1^{\ominus}\,(J/mol) =$$
$$-177650 + 99.4T \quad [29] \tag{3}$$

$$\Delta G = \Delta G^{\ominus} + RT \ln \frac{a_{(s)}}{w_{[i]} \cdot f_i \cdot w_{[j]} \cdot f_j} \tag{4}$$

$$\lg f_i = e_i^i w_{[i]} + \sum e_i^j w_{[j]} \tag{5}$$

where $a_{(s)}$ is the activity of the inclusion (here, $a_{(s)}$= 1), $w_{[i]}$ and $w_{[j]}$ are the mass percentages of different elements, f_i and f_j are the activity coefficients of elements i and j, respectively, and e_i^i and e_i^j are the interaction coefficients.

The inclusions can be formed in a nonstandard state, which can be derived from Eq. (5) using the relevant interaction coefficients listed in Table 2. The calculated Gibbs free energies of the different types of inclusions in these entropic alloys are presented in Fig. 6. It is clear that the ΔG values for these reactions all decrease with temperature and cross the line of $\Delta G = 0$ for Al_2O_3 and MnS inclusions, while $\Delta G < 0$ for HfO_2 for the entire temperature range. Moreover, Mo addition slightly increases the formation temperature of Al_2O_3 inclusions compared with that in Ref.-HEA, as shown in Fig. 6(a). The formation temperature of Al_2O_3 inclusions is
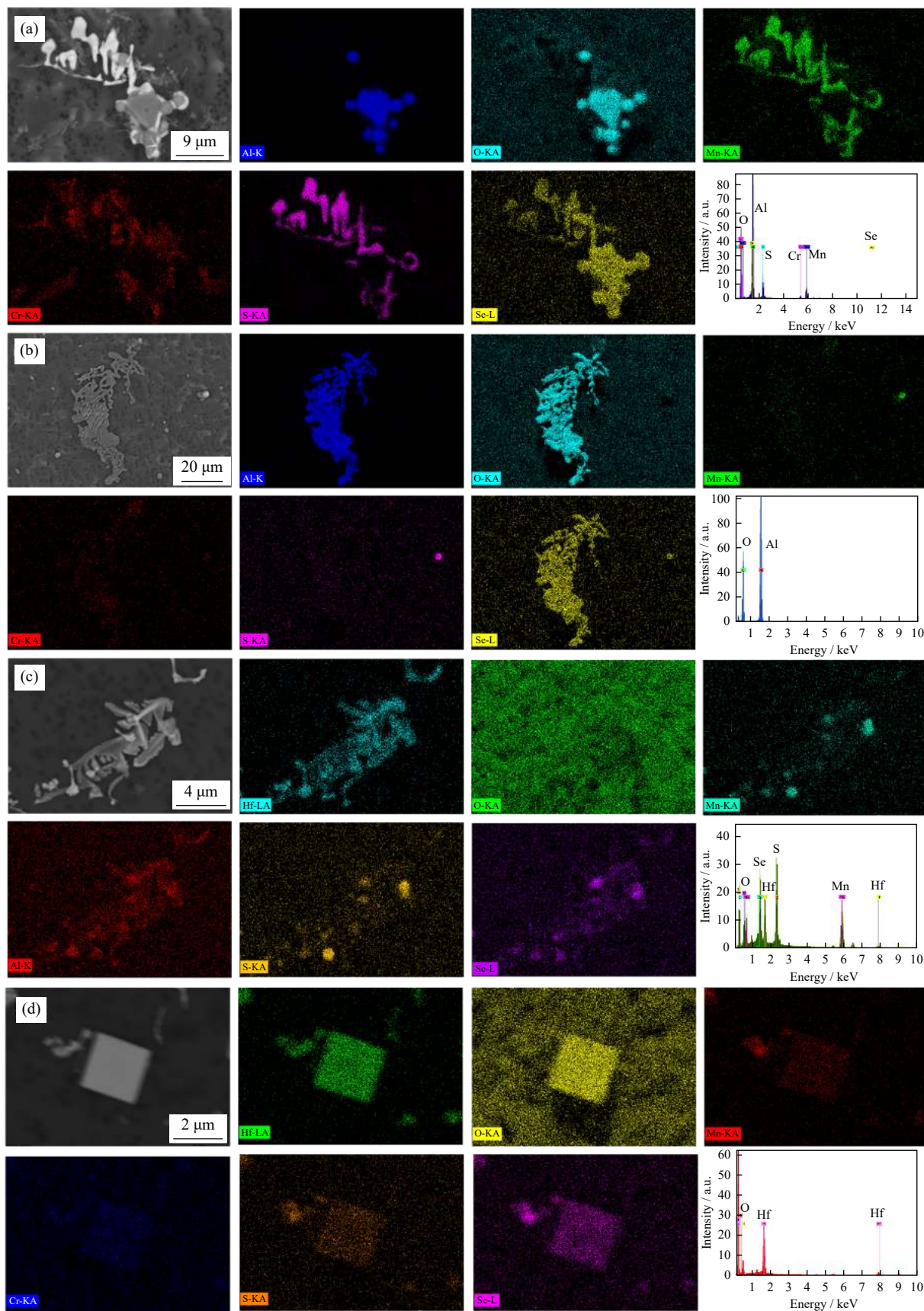
Fig. 4.   Elemental mapping of typical inclusions in three HEAs: (a) Ref.-HEA; (b) Mo-HEA; (c, d) Hf-HEA.

higher in Ref.-HEA and Mo-HEA than in Hf-HEA. From this perspective of ΔG, HfO_2 is more easily formed in Hf-HEA than the Al_2O_3 inclusions. This shows good agreement with previous work that Hf has oxide formation energies lower than Al [32]. The formation temperature of MnS decreases in the order of Ref.-HEA, Mo-HEA, and Hf-HEA.
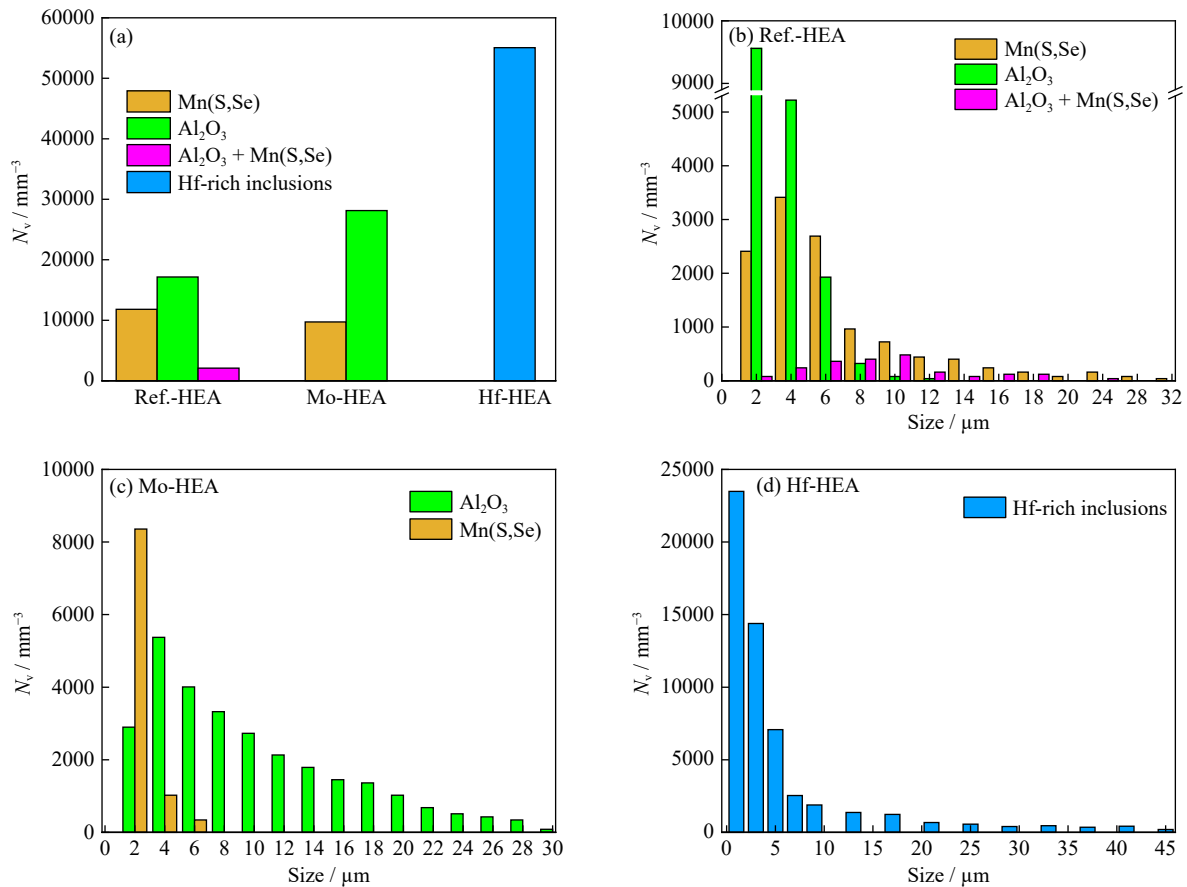
1644

Int. J. Miner. Metall. Mater., Vol. 31, No. 7, Jul. 2024

Fig. 5. (a) Number density of inclusions in three entropic alloys and particle size distributions of different types of inclusions in (b) Ref.-HEA, (c) Mo-HEA, and (d) Hf-HEA.

Table 2. First-order activity interaction coefficients used in this study [28,30–31]

Element i	Element j										
	Co	Cr	Fe	Mn	Ni	Mo	Hf	Al	S	O	N
Al	0.03	0.0096	−0.003	−0.004	−0.029		−0.004	0.043	0.035	−1.98	0.015
Hf			−0.016	−0.013	−0.075		0.007	−0.055	−0.27	−3.2	−7.262
Mn	−0.0036	0.0039		0	−0.0072	0.0046		−0.012	−0.048	−0.083	−0.091
O	0.008	−0.055	0.036	−0.021	0.006	0.005	−0.28	−1.17	−0.133	−0.17	−0.14
S	0.0026	−0.0105	0.005	−0.026		0.0027	−0.045	0.041	−0.046	−0.27	0.01

These calculation results show that Al_2O_3 and HfO_2 inclusions formed in the liquid HEA melt and MnS inclusions formed during the solidification process.

To further corroborate the thermodynamic analysis of inclusion formation, the equilibrium products of inclusions in different HEAs were calculated using FactSage 8.1 with the FactPS, FSstel, and FToxid databases. The results are shown in Fig. 7. It is clear that Al_2O_3 inclusions form in the liquid Ref.-HEA and Mo-HEA, and their amount is slightly larger in Mo-HEA. This result also aligns with the observed number density of inclusions in these two alloys, as displayed in Fig. 5(a). Moreover, HfO_2 inclusions are stable oxides in Hf-HEA, where Al_2O_3 inclusions are not formed. The amount of HfO_2 inclusions in Hf-HEA is approximately three or four times more than those of Al_2O_3 in Ref.-HEA and Mo-HEA. The precipitation temperature of MnS in Ref.-HEA and Mo-HEA is lower than the solidus temperature of the alloy

(1383°C), which agrees well with the results in Fig. 6(b). Note that HfS_2 inclusions are formed instead of MnS in Hf-HEA. However, some MnS was observed in this alloy, which was possibly due to the non-equilibration solidification process of Hf-HEA. The early-formed oxide inclusions can serve as heterogeneous nucleation sites for the precipitation of MnS on the surface of oxides.

To better understand the effect of Hf on the formation of Al_2O_3 and HfO_2 inclusions, equilibrium calculations were performed under different Hf and Al contents, and the results are shown in Fig. 7(b). It is obvious that Al_2O_3 inclusions are stable oxides without Hf addition, and the amount of Al_2O_3 inclusions gradually decreases with increasing Hf content, whereas that of HfO_2 inclusions increases. When the Hf content is greater than 0.08wt%, Al_2O_3 inclusions cannot exist in the melt where only HfO_2 inclusions are stable oxides. With a further increase in the Hf content, the amount of HfO_2 inclu-
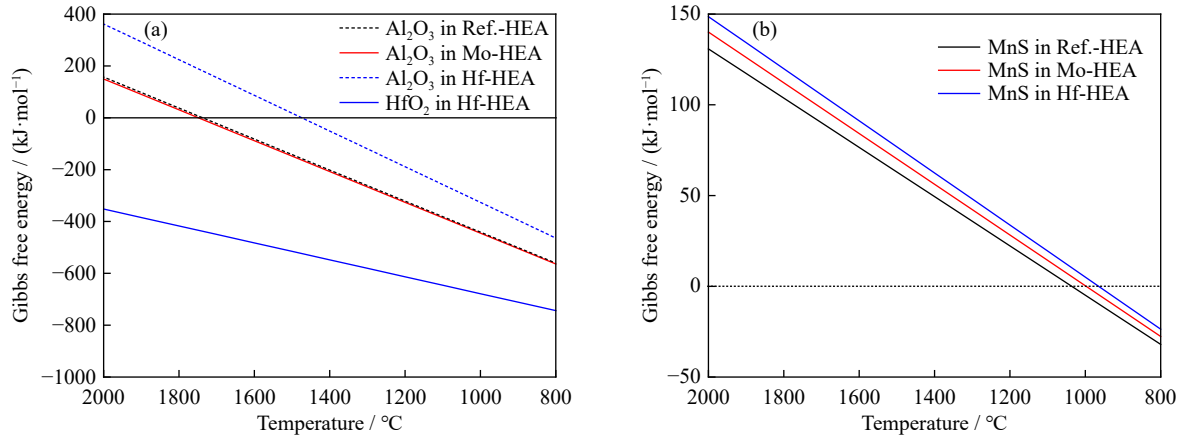
Fig. 6.   Gibbs free energy of the formation of (a) Al$_2$O$_3$ and HfO$_2$ inclusions and (b) MnS in the proposed entropic alloys.
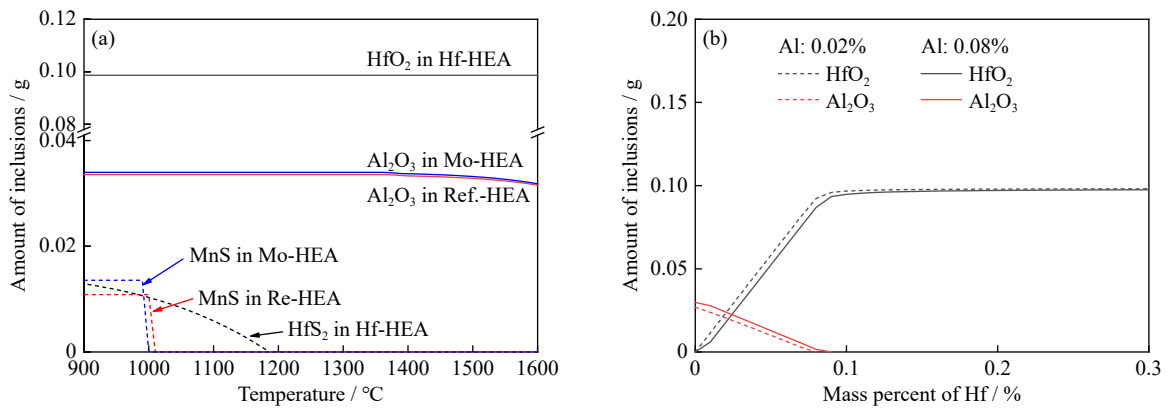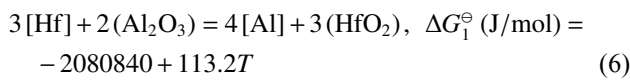

Fig. 7.   (a) Formation of inclusions in different HEAs at an equilibrium state and (b) the effect of Al and Hf contents on inclusion formation in Hf-HEA.

sions remains constant, which can be explained by the fact that all O in the melt is consumed by the formation of HfO$_2$ inclusions. Based on the calculations, it is reasonable to conclude that Hf in liquid HEA melt will react with Al$_2$O$_3$ inclusions because Hf is more reactive than Al; the possible reaction can be expressed by Eq. (6). Also, the same tendency can be found at higher Al contents, and a relatively higher Hf content is required for the complete reduction of Al$_2$O$_3$ inclusions. Filip *et al.* [33] observed that HfO$_2$ inclusions were found on the boundaries of Al$_2$O$_3$ phases because Hf atoms can replace Al atoms in Al$_2$O$_3$ oxides in Hf-containing superalloys, which validates these calculation results. This phenomenon can also be explained by the fact that HfO$_2$ inclusions were found instead of Al$_2$O$_3$ inclusions in Nb–Si-based alloys containing 2% Al and Hf [34]. Thus, the formation of inclusions in HEAs is dominated by active elements (in particular, Hf and Al).

$$3[\text{Hf}] + 2(\text{Al}_2\text{O}_3) = 4[\text{Al}] + 3(\text{HfO}_2), \ \Delta G_1^{\ominus} \ (\text{J/mol}) =$$
$$-2080840 + 113.2T \tag{6}$$

3.3. Nucleation, growth and collision behavior of inclusions

The Gibbs free energy of inclusions can only show their formation possibilities. During the formation process of these inclusions, the critical supersaturation degree is an important

factor, which means that nucleation would not occur until the required supersaturation of the elements is achieved. The inclusion morphology change after nucleation is closely associated with supersaturation. Based on Turpin and Elliott [35], the critical supersaturation degree of inclusions, $S = K/K_e$, in terms of free energy, $\Delta G_{\text{hom}}^{\text{crit}}$, for homogeneous nucleation of inclusions is given by Eq. (7). Under the critical supersaturation conditions, the radius of inclusions, r^*, can be expressed by Eq. (8).

$$\Delta G_{\text{hom}}^{\text{crit}} = -2.7v\left(\frac{\sigma^3}{kT\lg A}\right)^{1/2} = -RT\ln(K/K_e) \tag{7}$$

$$r^* = -\frac{2\sigma v}{\Delta G_{\text{hom}}^{\text{crit}}} \tag{8}$$

where v is the molar volume of inclusions (m^3·mol^{-1}), the value of which for Al$_2$O$_3$ is 2.56×10^{-5} m^3·mol^{-1} [36], that for HfO$_2$ is 2.17×10^{-5} m^3·mol^{-1} [37], and that for MnS is 2.2×10^{-5} m^3·mol^{-1} [38]; σ is the interfacial energy between the matrix and the inclusions; k is Boltzmann's constant (1.38×10^{-23} J/K); T is the temperature (K); A is the frequency factor (m^{-3}·s^{-1}), the value of which for Al$_2$O$_3$ is 10^{32} m^{-3}·s^{-1} [39], that for HfO$_2$ is 10^{33} m^{-3}·s^{-1} [39], and that for MnS is 10^{42} m^{-3}·s^{-1} [38]; K and K_e are the reaction constant and equilibrium constant of the inclusion formation reaction, respectively.

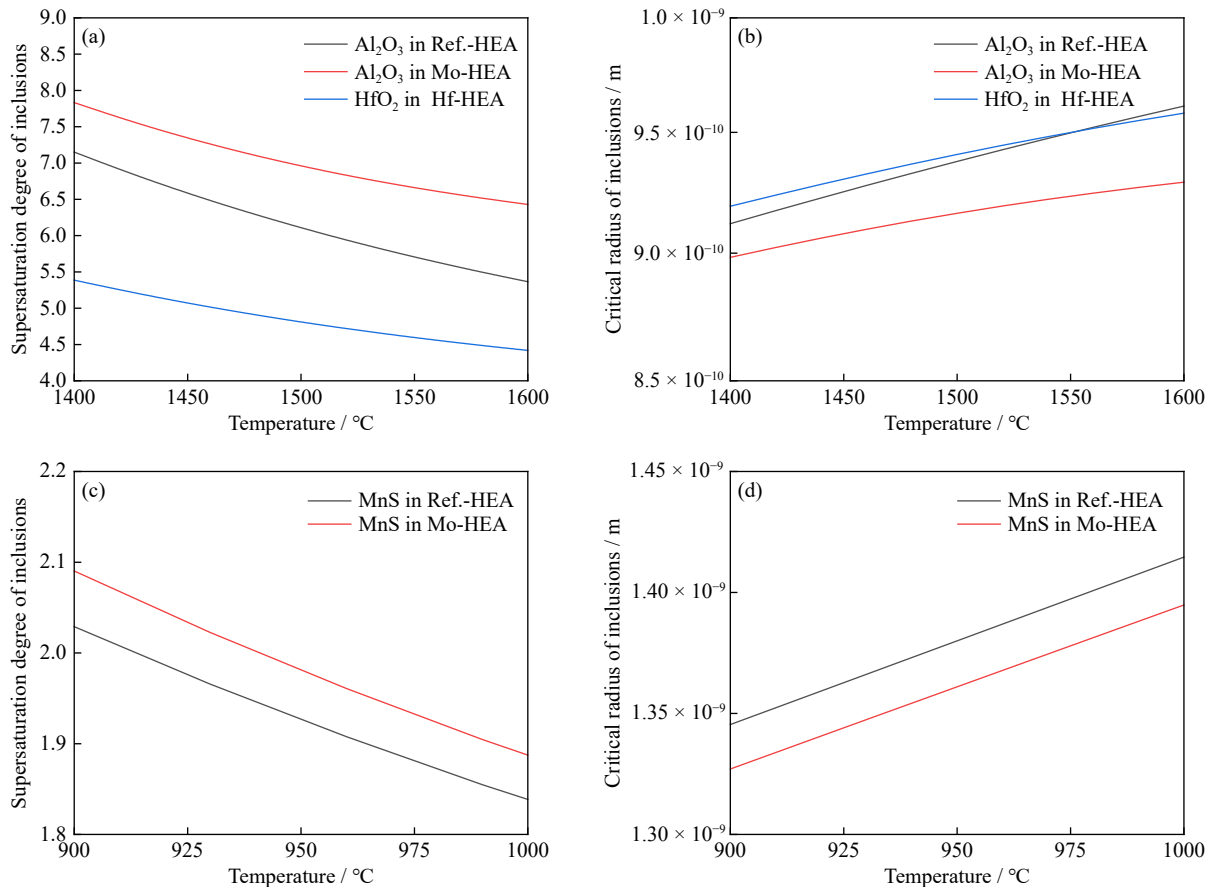The supersaturation degree of the different inclusions and

Fig. 8.   Calculated supersaturation and critical radius of (a, b) different oxide inclusions and (c, d) MnS inclusions.

critical inclusion sizes are presented in Fig. 8. HfO_2 inclusions can nucleate homogeneously at a smaller degree of supersaturation compared with Al_2O_3, and Al_2O_3 inclusions in Mo-HEA have the largest supersaturation degree among the three alloys. In terms of sulfide content, the supersaturation degree of MnS inclusions in Ref.-HEA is lower than that in Mo-HEA. The critical radius of inclusions shows the opposite tendency with respect to the supersaturation degree. Under the same melting conditions, dendritic inclusions can be formed at a lower critical supersaturation degree, which can be employed to explain the presence of dendritic MnS and HfO_2 inclusions. Moreover, it was reported that a supersaturated zone with a suitable gradient of supersaturation degree is required to conduct the dendritic growth of nucleation; if not, the nuclei would grow spherically [40]. In applying solidification theory, Steinmetz and Lindenberg [41] proposed a law of inclusion morphology change in terms of free energy balance between interfacial free energy (σ) and formation energy (ΔH) of inclusions. Spherical inclusions will form under the condition of high enough σ compared with ΔH. For dendritic growth, the magnitude of ΔH is higher than σ, i.e., the crystalline structure can behave as the decisive factor in determining the shape of the inclusion. For MnS inclusions, which belong to the cubic crystalline structure, they will grow with an octahedral morphology. Al_2O_3 and HfO_2 inclusions belong to rhombic (polyhedral) and cubic (tetragonal) crystalline systems. Regarding the dendritic inclusions, they have a transitional morphology that failed to grow into an oc-

tahedral/polyhedral/tetragonal morphology. Along with the supersaturation degree and inclusion morphology change, Fig. 9 displays the presence of different inclusion morphologies. During the initial stage of solidification, spherical inclusions will form under a high supersaturation degree. With the decreasing supersaturation degree, the inclusion morphologies evolve from spherical, via dendrites, to octahedral/polyhedral/tetragonal shapes. A deeper understanding of the relationship between the morphology and the supersaturation degree of inclusions can be considered in future work.
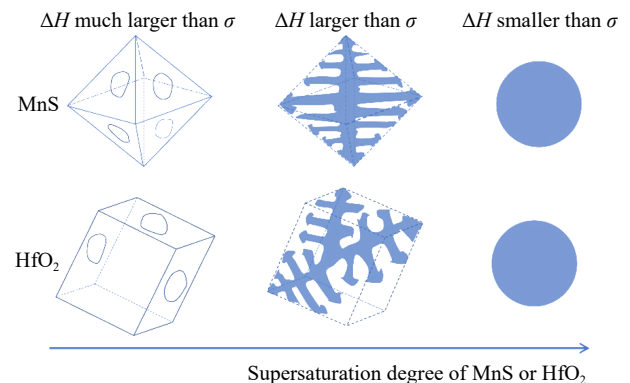

Fig. 9.   Morphological changes of inclusions as a function of supersaturation degree.

In general, the size of inclusions in HEA can be affected by nucleation, growth by element diffusion, and aggregation by collision. The number of collisions per unit volume and

unit time between two inclusions with number densities n_i and n_j is given as Eq. (9). Expressions for W_{ij}^B, W_{ij}^T, and W_{ij}^S are given by Eqs. (10)–(12) [42–44]:

$$N_{ij} = (W_{ij}^B + W_{ij}^T + W_{ij}^S)n_i n_j \qquad (9)$$

$$W_{ij}^B = \frac{2kT}{3\mu}\left(\frac{1}{r_i} + \frac{1}{r_j}\right)(r_i + r_j) \qquad (10)$$

$$W_{ij}^T = 1.3\alpha\sqrt{\frac{\pi\varepsilon\rho_{HEA}}{\mu}}(r_i + r_j)^3 \qquad (11)$$

$$W_{ij}^S = \frac{2\pi g(\rho_{HEA} - \rho_{NMI})}{9\mu}(r_i + r_j)^3 \left|r_i - r_j\right| \qquad (12)$$

where W_{ij}^B represents Brownian collisions; W_{ij}^T represents turbulent collisions; W_{ij}^S represents Stokes collisions; n_i and n_j are the numbers of colliding inclusions with radii r_i and r_j, respectively. k is the Boltzmann constant (1.38×10^{-23} J/K); T is the temperature (K); μ is the dynamic viscosity of the HEA melt; α is the coagulation coefficient; ε is the turbulent energy dissipation rate (in this work, 0.01 m^2/s^3 [25]); ρ_{NMI} is the density of inclusion, and ρ_{HEA} is the density of the proposed HEA (here, $\rho_{Al_2O_3}$ is 3900 kg/m^3, ρ_{HfO_2} is 9680 kg/m^3 [45]); g is the gravitational acceleration (9.81 $m \cdot s^{-2}$).

Previous results showed that the contribution of Brownian collisions to the total collision volume can be ignored because W_{ij}^B is several orders of magnitude lower than W_{ij}^T and W_{ij}^S [44,46]. Moreover, the total collision volume is domin-

antly influenced by turbulent collisions because Stokes collisions are highly associated with the size difference of inclusions. For turbulent collisions, the inclusion agglomeration potency in the liquid melt is related to the coagulation coefficient, which can be expressed as Eq. (13) [25,44].

$$\alpha = 0.727\left(\mu r_i^3 \frac{\sqrt{\rho_{HEA}\varepsilon/\mu}}{24\pi a^2\gamma_{IM}}\right)^{-0.242} \qquad (13)$$

where a is the distance between the anion and cation in a specific inclusion phase (2.8×10^{-10} m for Al_2O_3 [47] and 7.8×10^{-11} m for HfO_2 [48]) and γ_{IM} is the interfacial energy between the inclusion particle and liquid HEA, which is calculated by Thermo-Calc software.

In the previous section, agglomerated Al_2O_3 and HfO_2 inclusions were found in the proposed entropy alloys and showed different inclusion size ranges. The agglomeration potency of different inclusions can be influenced by the physical parameters of the liquid alloy and inclusions. The physical parameters of the liquid alloy were calculated by Thermo-Calc 2022a with the TCNI11 database, and the results are presented in Fig. 10. It is observed that only the interfacial energies between inclusions and liquid HEA increase slightly, while the surface tension, density, and dynamic viscosity of HEAs all decrease with increasing temperature. Specifically, the interfacial energy between Al_2O_3 and Mo-HEA is higher than that between HfO_2 and Hf-HEA, and that between Al_2O_3 and Ref.-HEA has the smallest value. The
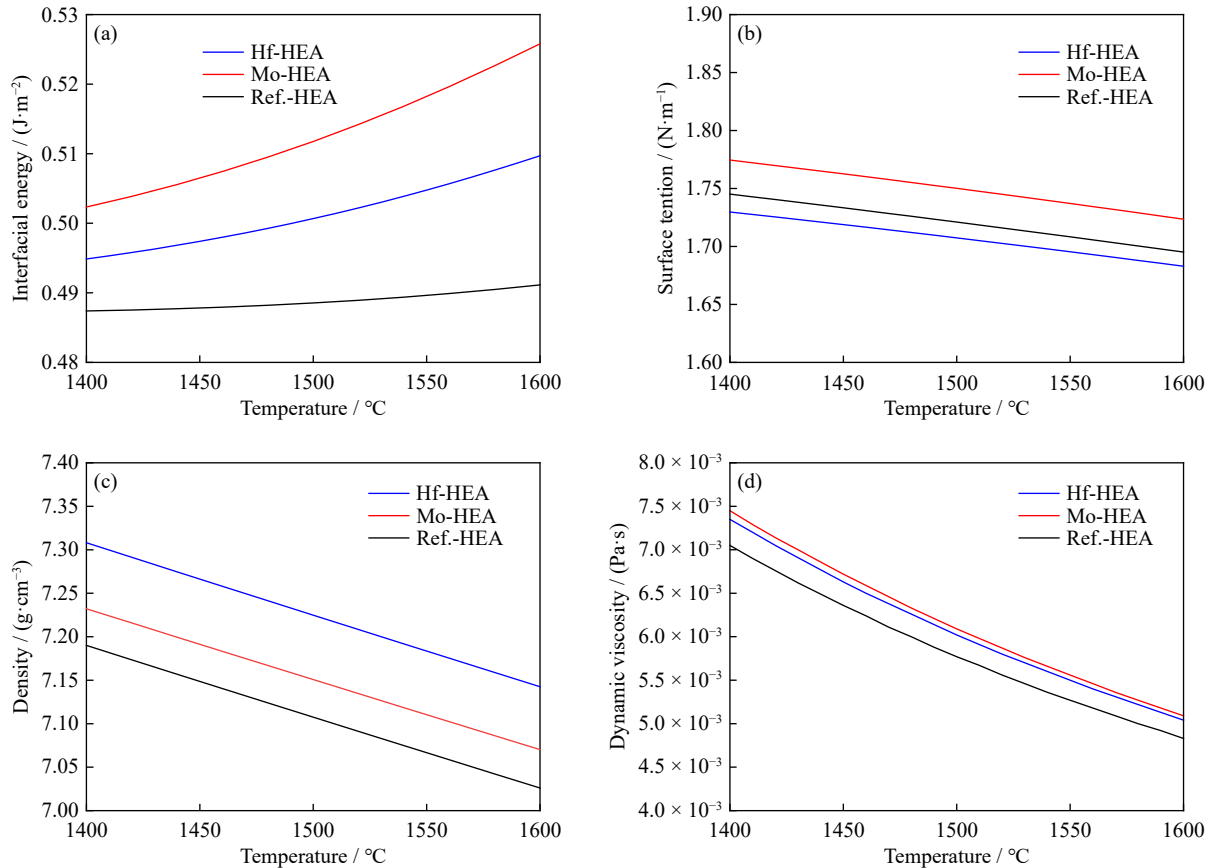

Fig. 10. Calculated physical parameters of the proposed entropy alloys: (a) interfacial energy between the inclusion and liquid alloy, (b) surface tension, (c) density, and (d) dynamic viscosity.

surface tensions of Ref.-HEA and Hf-HEA are close but a bit smaller than that of Mo-HEA. It has been reported that the attractive capillary force between two inclusions increased slightly with decreasing surface tension [44]. Alternatively, other researchers reported that the surface tension of melt alone hardly affected the attractive force of inclusions [49]. In this case, a joint influence of other factors need to be considered. The density shows a decreasing trend of Hf-HEA, Mo-HEA, and Ref.-HEA. According to the turbulent collision and Stokes collision mechanisms [42], a larger melt density and larger density difference between the melt and inclusions result in a larger inclusion collision tendency. It should also be noted that the Stokes collision effect can be greater only when the size difference between the two colliding inclusions is large [50], which demonstrates that the Stokes collision can be applied to larger inclusions. Thus, the agglomeration potency of Al_2O_3 inclusions in Mo-HEA can be larger than that in Ref.-HEA in terms of HEA density. Moreover, Mo-HEA has a slightly higher dynamic viscosity than Hf-HEA, with Ref.-HEA having the lowest value. Generally, the lower the viscosity value of the HEA melt, the easier it is for the inclusions to form aggregates. However, the viscosity values of HEA show an opposite tendency with the observed inclusion size. The combined physical parameters of liquid HEA were used to calculate the coagulation coefficient and collision-agglomeration potency, and the results are plotted in Fig. 11.
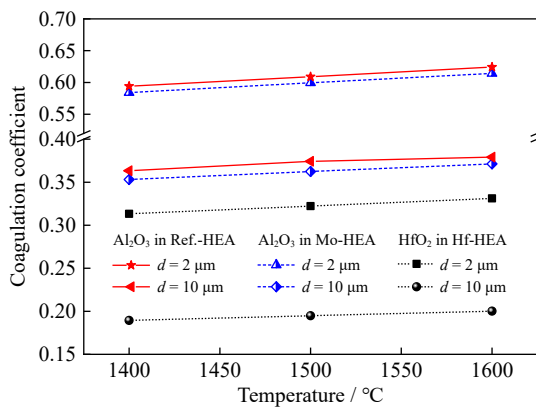

Fig. 11. Calculated coagulation coefficients of Al_2O_3 and HfO_2 inclusions in the proposed entropy alloys.
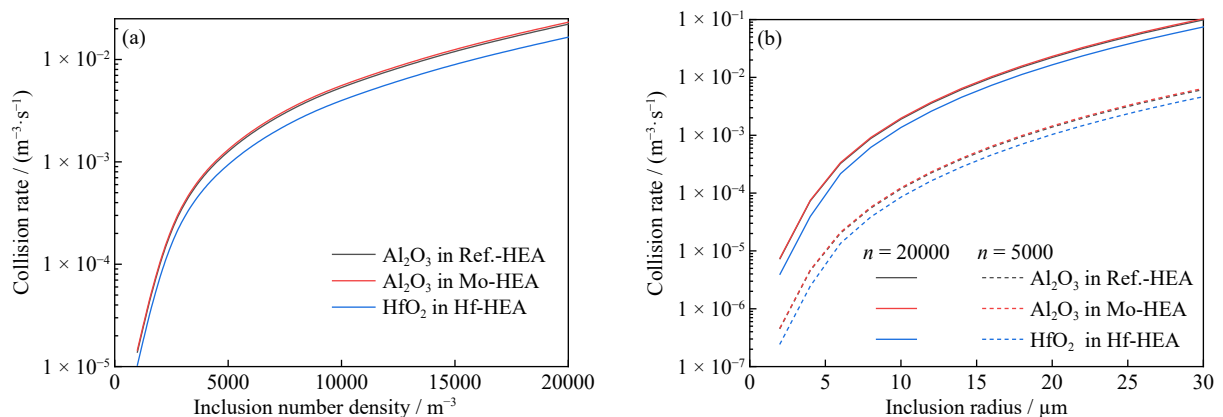
Inclusion sizes (d) were fixed at 2 and 10 μm for both Al_2O_3 and HfO_2 inclusions. The coagulation coefficient of different inclusions slightly increases with increasing temperature due to the influence of the physical parameters of liquid HEA. In addition, small-sized inclusions show a larger coagulation coefficient than the large-sized ones. Furthermore, the coagulation coefficients of Al_2O_3 in Mo-HEA and Ref.-HEA are larger than that of HfO_2 in Hf-HEA, implying that the calculated coagulation coefficients do not agree with the size ranges of Al_2O_3 and HfO_2 inclusions in different HEA alloys. In addition, the coagulation coefficients of Al_2O_3 inclusions are slightly smaller in Mo-HEA than in Ref.-HEA; such a tendency is slightly different from the experimental results.

Except for the influence of the physical parameters of alloys on inclusion agglomeration, inclusion number density is another crucial factor that cannot be ignored. This is because a larger number density of inclusions can increase the collision frequency between inclusions of various sizes, which favors the formation of large-sized inclusions. The effect of the number density on the collision rate of different types of inclusions is depicted in Fig. 12. For this calculation, the diameter of inclusion i is fixed at 2 μm, and the number density values of inclusions i and j are the same ($n_i = n_j$). It is observed that under the condition of the same diameter and number density of inclusions, the collision rate of Al_2O_3 inclusions in Mo-HEA is higher than that in Ref.-HEA, while that of HfO_2 in Hf-HEA is the smallest among the three alloys (Fig. 12(a)). This tendency is inconsistent with the calculated coagulation coefficients of Al_2O_3 and HfO_2 inclusions in different alloys. Also, the collision rate significantly increases with an increase in the number density of inclusions. The influence of the number density of inclusions can be clearly observed in Fig. 12(b); the collision rate of HfO_2 inclusions in Hf-HEA under a number density (n) of 20000 is more than 10 times that of Al_2O_3 inclusions in Mo-HEA and Ref.-HEA under a number density of 5000. However, the collision rate of Al_2O_3 inclusions is approximately 1.5 times that of HfO_2 inclusions under the same number density. This shows that the number density has a more pronounced effect on the collision rate than the inclusion type. Based on the experimental results in Fig. 5(a), the number density of HfO_2

Fig. 12.   Effect of (a) inclusion number density and (b) inclusion radius on the collision rate of inclusions.

inclusions in Hf-HEA is approximately two or three times higher than those of Al_2O_3 inclusions in Mo-HEA and Ref. -HEA. Considering the number density difference in HfO_2 and Al_2O_3 inclusions, the collision rate of HfO_2 inclusions can be higher than that of Al_2O_3 inclusions. This might be the reason for the larger size range of HfO_2 inclusions in Hf-HEA compared with Al_2O_3 inclusions in Mo-HEA and Ref. -HEA.

4. Conclusions

This work examined the effect of refractory elements (Hf and Mo) addition on inclusion formation in Co-based dual-phase HEAs. The appearance of different types of inclusions was represented, and the formation mechanisms were analyzed by thermodynamic calculations. The main findings can be summarized as follows:

(1) The stable oxide inclusions in Ref.-HEA and Mo-HEA are Al_2O_3, and the size range of these inclusions is significantly higher in Mo-HEA. Hf-rich inclusions are the stable oxides in Hf-HEA, which have the largest number density and size ranges compared with Al_2O_3 inclusions in Ref.-HEA and Mo-HEA. Dendritic Mn(S,Se) inclusions were observed in Ref.-HEA, whereas globular inclusions were more commonly found in Mo-HEA and Hf-HEA.

(2) Based on thermodynamic calculations, HfO_2 is more stable than Al_2O_3, and Al_2O_3 can be reduced by Hf. Moreover, Mo addition does not affect inclusion types but can lead to different inclusion characteristics by affecting the physical parameters of the HEA melt.

(3) The coagulation coefficients and observed size ranges of Al_2O_3 in Mo-HEA and Ref.-HEA were jointly affected by the interfacial energy, surface tension, and density of the HEA melt. Moreover, the coagulation coefficient and collision rate of Al_2O_3 inclusions are higher than those of HfO_2 inclusions. The larger size range of HfO_2 inclusions found experimentally can be explained by their larger number density, which is the main factor that affects their agglomeration behavior.

Acknowledgements

Conflict of Interest

References

[1] D.B. Miracle and O.N. Senkov, A critical review of high entropy alloys and related concepts, *Acta Mater.*, 122(2017), p. 448.

[2] Z. Cheng, S.Z. Wang, G.L. Wu, J.H. Gao, X.S. Yang, and H.H. Wu, Tribological properties of high-entropy alloys: A review, *Int. J. Miner. Metall. Mater.*, 29(2022), No. 3, p. 389.

[3] Y.Q. Wu, P.K. Liaw, R.X. Li, *et al.*, Relationship between the unique microstructures and behaviors of high-entropy alloys, *Int. J. Miner. Metall. Mater.*, 31(2024), No. 6, p. 1350.

[4] P.J. Shi, W.L. Ren, T.X. Zheng, *et al.*, Enhanced strength–ductility synergy in ultrafine-grained eutectic high-entropy alloys by inheriting microstructural lamellae, *Nat. Commun.*, 10(2019), No. 1, art. No. 489.

[5] Z. Li, K.G. Pradeep, Y. Deng, D. Raabe, and C.C. Tasan, Metastable high-entropy dual-phase alloys overcome the strength-ductility trade-off, *Nature*, 534(2016), No. 7606, p. 227.

[6] Y. Zhang, M. Zhang, D.Y. Li, *et al.*, Compositional design of soft magnetic high entropy alloys by minimizing magnetostriction coefficient in $(Fe_{0.3}Co_{0.5}Ni_{0.2})_{100-x}(Al_{1/3}Si_{2/3})_x$ system, *Metals*, 9(2019), No. 3, art. No. 382.

[7] M. Zhang, J.X. Hou, H.J. Yang, *et al.*, Tensile strength prediction of dual-phase $Al_{0.6}CoCrFeNi$ high-entropy alloys, *Int. J. Miner. Metall. Mater.*, 27(2020), No. 10, p. 1341.

[8] W. Wang, Z.Y. Hou, R. Lizárraga, *et al.*, An experimental and theoretical study of duplex fcc+hcp cobalt based entropic alloys, *Acta Mater.*, 176(2019), p. 11.

[9] W.H. Liu, J.Y. He, H.L. Huang, H. Wang, Z.P. Lu, and C.T. Liu, Effects of Nb additions on the microstructure and mechanical property of CoCrFeNi high-entropy alloys, *Intermetallics*, 60(2015), p. 1.

[10] T.T. Shun, L.Y. Chang, and M.H. Shiu, Microstructures and mechanical properties of multiprincipal component CoCrFeNiTi_x alloys, *Mater. Sci. Eng. A*, 556(2012), p. 170.

[11] H. Ren, R.R. Chen, X.F. Gao, *et al.*, Phase formation and mech-

1650

Int. J. Miner. Metall. Mater., Vol. 31, No. 7, Jul. 2024

anical features in $(AlCoCrFeNi)_{100-x}Hf_x$ high-entropy alloys: The role of Hf, *Mater. Sci. Eng. A*, 858(2022), art. No. 144156.

[12] T.T. Shun, L.Y. Chang, and M.H. Shiu, Microstructure and mechanical properties of multiprincipal component CoCrFeNiMo$_x$ alloys, *Mater. Charact.*, 70(2012), p. 63.

[13] S. Haas, A.M. Manzoni, F. Krieg, and U. Glatzel, Microstructure and mechanical properties of precipitate strengthened high entropy alloy $Al_{10}Co_{25}Cr_8Fe_{15}Ni_{36}Ti_6$ with additions of hafnium and molybdenum, *Entropy*, 21(2019), No. 2, art. No. 169.

[14] A. Gali and E.P. George, Tensile properties of high- and medium-entropy alloys, *Intermetallics*, 39(2013), p. 74.

[15] F. Otto, N.L. Hanold, and E.P. George, Microstructural evolution after thermomechanical processing in an equiatomic, single-phase CoCrFeMnNi high-entropy alloy with special focus on twin boundaries, *Intermetallics*, 54(2014), p. 39.

[16] F. Otto, A. Dlouhý, K.G. Pradeep, *et al.*, Decomposition of the single-phase high-entropy alloy CrMnFeCoNi after prolonged anneals at intermediate temperatures, *Acta Mater.*, 112(2016), p. 40.

[17] B. Gludovatz, A. Hohenwarter, D. Catoor, E.H. Chang, E.P. George, and R.O. Ritchie, A fracture-resistant high-entropy alloy for cryogenic applications, *Science*, 345(2014), No. 6201, p. 1153.

[18] K.P. Yu, S.H. Feng, C. Ding, P. Yu, and M.X. Huang, Improving anti-corrosion properties of CoCrFeMnNi high entropy alloy by introducing Si into nonmetallic inclusions, *Corros. Sci.*, 208(2022), art. No. 110616.

[19] Y. Wang, Y.L. Li, W. Wang, *et al.*, Effect of manufacturing conditions and Al addition on inclusion characteristics in Co-based dual-phase high entropy alloy, *Metall. Mater. Trans. A*, 54(2023), No. 7, p. 2715.

[20] G. Qin, R.R. Chen, H.T. Zheng, *et al.*, Strengthening FCC-CoCrFeMnNi high entropy alloys by Mo addition, *J. Mater. Sci. Technol.*, 35(2019), No. 4, p. 578.

[21] L.M. Ma, X.X. Tang, L.N. Jia, S.N. Yuan, J.R. Ge, and H. Zhang, Influence of Hf contents on interactions between Nb-silicide based alloys and yttria moulds during directional solidification, *Int. J. Refract. Met. Hard Mater.*, 33(2012), p. 87.

[22] O. Benafan, G.S. Bigelow, A. Garg, R.D. Noebe, D.J. Gaydosh, and R.B. Rogers, Processing and scalability of NiTiHf high-temperature shape memory alloys, *Shape Mem. Superelasticity*, 7(2021), No. 1, p. 109.

[23] Y.Z. Zhou, A. Volek, and R.F. Singer, Influence of solidification conditions on the castability of nickel-base superalloy IN792, *Metall. Mater. Trans. A*, 36(2005), No. 3, p. 651.

[24] I.V. Belyaev, V.E. Bazhenov, A.V. Kireev, and A.V. Moiseev, Nonmetallic inclusions in a new alloy for single-crystal permanent magnets, *Arch. Foundry Eng.*, 18(2018), No. 2, p. 11.

[25] W. Wang, Y. Wang, W. Mu, *et al.*, Inclusion engineering in Co-based duplex entropic alloys, *Mater. Des.*, 210(2021), art. No. 110097.

[26] C.L. Qiu and X.H. Wu, High cycle fatigue and fracture behaviour of a hot isostatically pressed nickel-based superalloy, *Philos. Mag.*, 94(2014), No. 3, p. 242.

[27] H. Ohta and H. Suito, Activities of MnO in CaO–SiO_2–Al_2O_3–MnO (<10 Pct)–Fe_tO(<3 pct) slags saturated with liquid iron, *Metall. Mater. Trans. B*, 26(1995), No. 2, p. 295.

[28] Y. Haruna, *Removal of Inclusions from Cast Superalloy Revert* [Dissertation], University of British Columbia, Vancouver, 1994.

[29] Y.Z. Luo, J.M. Zhang, Z.M. Liu, C. Xiao, and S.Z. Wu, *In situ* observation and thermodynamic calculation of MnS in 49MnVS3 non-quenched and tempered steel, *Acta Metall. Sin. Engl. Lett.*, 24(2011), No. 4, p. 326.

[30] T. Matsushita and K. Mukai, *Chemical Thermodynamics in Materials Science*: *From Basics to Practical Applications*, Springer, Singapore, 2018.

[31] S.B. Rumyantseva, B.A. Rumyantsev, V.N. Simonov, G.S. Sprygin, and V.N. Kashirtsev, Optimum deoxidation of a Kh65NVFT chromium–nickel alloy containing refractory metals, *Russ. Metall. Met.*, 2020(2020), No. 12, p. 1349.

[32] S. Takaya, T. Furukawa, G. Müller, *et al.*, Al-containing ODS steels with improved corrosion resistance to liquid lead–bismuth, *J. Nucl. Mater.*, 428(2012), No. 1-3, p. 125.

[33] R. Filip, M. Zagula-Yavorska, M. Pytel, J. Romanowska, M. Maliniak, and J. Sieniawski, The oxidation resistance of non-modified and Zr-modified aluminide coatings deposited by the CVD method, *Solid State Phenom.*, 227(2015), p. 361.

[34] H. Qian, *The Effect of Processing Parameters on Structure Evolution during Laser Additive Manufacturing and Post-processing of Niobium-Silicide Based Alloys* [Dissertation], University of Leicester, Leicester, 2021.

[35] M.L. Turpin and J.F. Elliott, Nucleation of oxide inclusions in iron melts, *J. Iron. Steel. Inst.*, 204(1966), p. 217.

[36] T. Gheno and B. Gleeson, Kinetics of Al_2O_3-scale growth by oxidation and dissolution in molten silicate, *Oxid. Met.*, 87(2017), No. 3, p. 527.

[37] J.A. Murdzek and S.M. George, Effect of crystallinity on thermal atomic layer etching of hafnium oxide, zirconium oxide, and hafnium zirconium oxide, *J. Vac. Sci. Technol. A*: *Vac. Surf. Films*, 38(2020), No. 2, art. No. 022608.

[38] D.L. You, S.K. Michelic, G. Wieser, and C. Bernhard, Modeling of manganese sulfide formation during the solidification of steel, *J. Mater. Sci.*, 52(2017), No. 3, p. 1797.

[39] D.L. You, S.K. Michelic, P. Presoly, J.H. Liu, and C. Bernhard, Modeling inclusion formation during solidification of steel: A review, *Metals*, 7(2017), No. 11, art. No. 460.

[40] N. Aritomi and K. Gunji, Morphology and formation mechanism of dendritic inclusions in iron and iron-nickel alloys deoxidized with silicon and solidified unidirectionally, *ISIJ Int.*, 19(1979), No. 3, p. 152.

[41] E. Steinmetz and H.U. Lindenberg, Morphology of inclusions during deoxidation (of Fe melts) with Al, *Arch. Eisenhuttenwes.*, 47(1976), p. 199.

[42] L.F. Zhang, S. Taniguchi, and K.K. Cai, Fluid flow and inclusion removal in continuous casting tundish, *Metall. Mater. Trans. B*, 31(2000), No. 2, p. 253.

[43] C.J. Xuan, A.V. Karasev, and P.G. Jönsson, Evaluation of agglomeration mechanisms of non-metallic inclusions and cluster characteristics produced by Ti/Al complex deoxidation in Fe-10mass% Ni alloy, *ISIJ Int.*, 56(2016), No. 7, p. 1204.

[44] W. Mu, N. Dogan, and K.S. Coley, Agglomeration of non-metallic inclusions at the steel/Ar interface: Model application, *Metall. Mater. Trans. B*, 48(2017), No. 4, p. 2092.

[45] O. Buiu, W. Davey, Y. Lu, I.Z. Mitrovic, and S. Hall, Ellipsometric analysis of mixed metal oxides thin films, *Thin Solid Films*, 517(2008), No. 1, p. 453.

[46] K.L. Chen, D.Y. Wang, D. Hou, T.P. Qu, J. Tian, and H.H. Wang, Effect of interfacial properties on agglomeration of inclusions in molten steels, *ISIJ Int.*, 59(2019), No. 10, p. 1735.

[47] K. Nakajima, W. Mu, and P.G. Jönsson, Assessment of a simplified correlation between wettability measurement and dispersion/coagulation potency of oxide particles in ferrous alloy melt, *Metall. Mater. Trans. B*, 50(2019), No. 5, p. 2229.

[48] C.Y. Chain, R.A. Quille, and A.F. Pasquevich, Ball milling induced solid-state reactions in the La_2O_3–HfO_2 ceramic system, *J. Alloys Compd.*, 495(2010), No. 2, p. 524.

[49] S. Kimura, K. Nakajima, and S. Mizoguchi, Behavior of alumina-magnesia complex inclusions and magnesia inclusions on the surface of molten low-carbon steels, *Metall. Mater. Trans. B*, 32(2001), No. 1, p. 79.

[50] M. Söder, P. Jönsson, and L. Jonsson, Inclusion growth and removal in gas-stirred ladles, *Steel Res. Int.*, 75(2004), No. 2, p. 128.